

Implementation of the spectral line-based weighted-sum-of-gray-gases model in the finite volume method for radiation modeling in internal combustion engines

Filip Jurić¹  | Pedro J. Coelho² | Peter Priesching³ | Neven Duić¹ | Stanislav Honus⁴ | Milan Vujanović¹

¹Faculty of Mechanical Engineering and Naval Architecture, University of Zagreb, Zagreb, Croatia

²IDMEC, Instituto Superior Técnico, Universidade de Lisboa, Lisbon, Portugal

³AVL List GmbH, Graz, Austria

⁴Faculty of Mechanical Engineering, VŠB-Technical University of Ostrava, Ostrava-Poruba, Czech Republic

Correspondence

Milan Vujanović, Faculty of Mechanical Engineering and Naval Architecture, University of Zagreb, Ivana Lučića 5, 10000 Zagreb, Croatia.
Email: milan.vujanovic@fsb.hr

Funding information

European Regional Development Fund, Operational Programme Competitiveness and Cohesion 2014–2020, Grant/Award Number: KK.01.1.1.04.0070

Summary

It is well-known that the pollutant formation processes and temperature distribution in various combustion systems that operate at high temperatures are influenced by radiation heat transport. Detailed modeling of radiation transport in internal combustion (IC) engines demands additional computational power, and hence the calculation of radiation phenomenon is not commonly applied in IC engines. At the same time, current operating conditions in IC engines consider high temperatures and recirculation of exhaust gases that enhance gas radiation. Therefore, the application of radiation models is needed to increase the correctness of radiative absorption, combustion characteristics, and the formation of pollutant emissions. In this paper, the implementation and validation of the spectral line-based weighted-sum-of-gray-gases (SLW) model for calculating soot and gas radiation are performed. The SLW model is implemented in the computational fluid dynamics code AVL FIRE by programmable user routines. The radiative transfer equation was calculated employing the finite volume method applicable for multiprocessing, moving meshes, and a mesh rezone procedure required for IC engine modeling. The validation of the SLW model is performed on one-dimensional geometric cases that include analytical results of radiation intensity, for which agreement within 10% of the relative error was achieved. Additionally, the SLW model is applied to compression ignition engine simulations, where the obtained results are compared with the measured pressure and concentrations of NO and soot emissions. The calculated heat losses through the wall boundary layer were around 12% of the total fuel energy, approximately 9.5% of the total fuel energy was lost due to the convective flow. 7%–8% of convection heat loss was due to the higher emission than absorption of participating CO₂ and H₂O gasses, and the rest are net soot losses. For the observed operating cases, the computational time is increased nearly double for SLW model than in the simulation without radiation. Finally, the results calculated using SLW indicate an improved agreement with the experimental mean pressure, temperature, soot, and NO concentrations compared to simulations without radiation.

KEYWORDS

gas radiation, internal combustion engine, participating media, radiative absorption, radiative heat transfer

1 | INTRODUCTION

It is well-known that radiative heat transfer is intensified at the high operating temperatures present in combustion systems.¹ A dominant share of total heat transfer is accomplished by radiation for systems that feature larger sizes, such as boilers, furnaces, and jet engines.² According to recent publications, the impact of radiation heat transport on pollutant formations needs to be considered if the correct calculation of emissions is demanded.³ Most pollutant formation models are affected by temperature distribution, which arises from the heat transfer calculation.⁴ Owing to that, it is necessary to correctly calculate radiative heat transfer for the participating radiative medium in combustion systems.⁵ In addition to developing complex numerical models, the increasing research in alternative fuels that feature lower emissions is present, such as research on alternative fuels in the transportation sector made from waste,⁶ torrefied biomass,⁷ biomass oils,⁸ and ammonia.⁹

Computational fluid dynamics (CFD) is a standard tool to simulate combustion systems and account for the effect of radiative heat transport on the temperature and its influence on the pollutants formation process.¹⁰ When the participation of the medium in the radiative heat transport is considered, the solution of the integrodifferential radiative transfer equation (RTE) is required.¹¹ A numerical approximation to solve the RTE has led to the development of numerous radiation models.¹² Thermal radiation is often neglected in internal combustion (IC) engines due to the relatively small size of the combustion chamber, but a few works have taken radiation into account.^{3,13–15} Even though it may have a relatively small impact on temperature, it affects the highly temperature-dependent NO emissions, as pointed out above.

In this work, the radiation model finite volume method (FVM) is employed to approximate the RTE. FVM radiation model, in combination with CFD software AVL FIRE, is modeled by user functions, which implementation was published on an IC engine¹⁴ and a furnace.¹⁶ One of the advantages of FVM model is its capability to model the impact of radiative heat transport in moving meshes as in IC engines, compared to the discrete transfer radiative method, which would be computationally demanding with mesh rezone.¹⁷ The FVM is a generalized method in CFD that applies to a wide range

of engineering projects that feature radiative heat transport.¹⁸ Compared to the line-by-line models, in FVM, spectral line properties of carbon dioxide (CO₂), water vapor (H₂O), and soot are required to be calculated.¹⁹ However, these models are too time-consuming for practical application due to the complex spectral dependence of the absorption coefficients of CO₂ and H₂O. Hence, the radiative heat exchange in participating media often relies on the utilization of global models to calculate the radiative properties of the medium.^{20,21}

The most recent work regarding absorption coefficient modeling was done on developing the radiative absorption coefficient models based on the weighted-sum-of-gray-gases model.²² Recently developed weighted-sum-of-gray-gases models mainly aim to determine the radiative heat transfer of the participating media in oxy-fuel combustion conditions.^{23,24}

In this work, the Spectral line-based Weighted-sum-of-gray-gases (SLW) model is used to calculate the radiative properties in IC engines. This is an improved version of the classical weighted-sum-of-gray-gases model that considers the spectral line properties of H₂O and CO₂.²⁵ Ozen and Selçuk²⁶ were the first to implement the discrete ordinates method along with the SLW model in CFD code. The implemented model performed an increased accuracy when the gas combustion was included, verifying that the spectral radiative properties of participating media are dominant in the overall radiative heat transport.

The SLW model was also employed for the three-dimensional (3D) combustion of partial-oxidation methane flame, where SLW provided valid results at sufficient computational demand.²⁷ Webb et al.²⁸ performed additional validation of SLW in a coal-fired furnace and revealed differences between gray and non-gray calculations. A comprehensive comparison between the weighted-sum-of-gray-gases method and the SLW model was performed by Ali et al.²⁹ in order to evaluate radiative transfer from a single participating gas at a uniform temperature and a non-isothermal mixture of gases inside a two-dimensional enclosure. Sun and Zhang³⁰ showed that different gray gases have completely different contributions in SLW model. In combination with different RTE solving models (FVM and P₁ approximation), different accuracies for the gray gases are obtained. The authors proposed a hybrid FVM/P₁ model combined with SLW and stated that further investigation of this

hybrid method is required. Other applications of the SLW model for two-dimensional calculations showed that the temperature field inside a radiant furnace contributed to inaccurate results of the radiative heat transfer through the medium.^{31–33} The first published investigation that analyzed radiative heat transfer in oxy-fuel combustion with the model based on SLW was performed by Ströhle,³⁴ where only the radiative absorption properties of gaseous H₂O and CO₂ were analyzed.

In the review paper,³⁵ the influence of radiative heat transfer in turbulent flames with the SLW model was investigated. It was concluded that the SLW model has a good perspective for engineering applications for calculating the radiative heat transfer of participating media. In another review paper,³⁶ a historical overview of the mathematical model, implementation, and application of the SLW model is given. Additional work was performed to investigate the SLW model compared to narrowband and wideband radiative absorption coefficient models in one-dimensional cases,³⁰ where the authors compared FVM and P1 models for solving the RTE in combination with the SLW model. The better accuracy was achieved with the FVM. Ozen and Selçuk³⁷ performed a sensitivity analysis of several gas radiative property models, including the SLW model, where the SLW and DOM demonstrated efficient and accurate simulations for determining energy source terms and wall intensities inside fluidized bed combustors. From the literature review, SLW radiative absorption model is imposed as adequate solution for accurate and computationally acceptable solutions and was therefore implemented in this work for further investigation of radiative heat transfer in IC engines.

In this paper, the SLW model is implemented in the CFD software AVL FIRE as a gas radiative heat transfer estimation computation approach for predicting the combined CO₂, H₂O, and soot absorption coefficient. The SLW was firstly validated against the analytical data for simple geometries. The predictive accuracy of the AVL FIRE code with the SLW model is assessed for a compression ignition engine operation that features a complex 3D moving mesh and rezone procedure computed on multi-processing units. According to the authors' knowledge, the SLW model was never employed in combination with FVM to model radiative heat transfer in IC engine applications. The combination of SLW and FVM constitutes a robust and computationally reasonable solution that applies to wide-range of complex industrial applications, such as moving meshes in IC engines. Additionally, very few papers^{3,15} account for non-gray thermal radiation using accurate models in IC engines, but they use accurate and time-consuming methods. Although thermal radiation in IC engines may play a relatively minor role for light-duty vehicles, the SLW/FVM can provide an

insight into its effect on emissions pollutant formation, such as NO_x and soot.

2 | MATHEMATICAL MODEL

In this work, the Reynolds-Averaged Navier-Stokes equations were solved using the *k-zeta-f* turbulence model. The *k-zeta-f* turbulence model is a robust turbulence model that allows the modeling of swirl motions inside IC engines and small wall distance values at boundary layers.³⁸ For calculating the gaseous phase, Eulerian specification of the fluid flow is assumed, for which the conservation equations of mass, momentum, and energy must be solved. Equation (1) describes energy conservation for the FVM, where the energy terms are integrated over the volume or each face of a control volume.

$$\frac{\partial}{\partial t}(\rho e) + u_i \frac{\partial}{\partial x_i}(\rho e) = \rho f_i u_i + \frac{\partial \tau_{ij} u_j}{\partial x_i} - \frac{\partial (u_i p)}{\partial x_i} \quad (1)$$

$$+ \frac{\partial}{\partial x_i} \left(\lambda \frac{\partial T}{\partial x_i} \right) + S_{rad},$$

where e is total energy, the first term on the left side represents the total energy rate, the second represents the total energy transfer across the control volume boundaries. The first term on the right side is the power of volume forces, and the second term is the surface power forces on the control volume boundaries. The third term on the right side is pressure forces, while the fourth term is the heat transfer rate through the control volume boundaries. At the end is the source term, which is described as the radiative heat source of participating media. The implemented radiation model and absorption coefficient model aim to determine the radiative heat source term.

2.1 | Radiative transfer calculation

The FVM radiation model was employed for the solution of RTE, as mentioned above. The FVM was considered only for absorption and emission phenomena. The participating medium absorbs the incident radiation, which is then augmented with the radiative emission of the medium, and scattering is neglected. The FVM features angular discretization that involves the calculation of the radiation intensity through the solution of a transport equation for each control angle. The absorption coefficient of the medium was computed with the SLW model, which requires a transport equation for each gray gas. The following equation describes the RTE:

$$\frac{dI_{lj}}{ds_l} = \kappa_j \left(a_j \frac{\sigma T^4}{\pi} - I_{lj} \right). \quad (2)$$

In Equation (2), the I_{lj} is the radiation intensity that propagates along s_l direction, l denotes the control angle, κ_j is the absorption coefficient, where j denotes the j^{th} gray gas for a mixture of H_2O and CO_2 and soot, and a_j denotes the combined gray gas weights of H_2O and CO_2 , which are calculated as the product of the two individual gray gas weights²⁵:

$$a_j = a_{\text{H}_2\text{O}} a_{\text{CO}_2}. \quad (3)$$

Equation (2) is required to be solved for all control angle $\Delta\Omega_l$, where the transient term was not considered as in previous IC engine research.^{3,15} The spatial discretization was carried out using the upwind scheme to calculate the radiation intensity at the downstream cell faces of a control volume. The marching procedure for solving the FVM equation was employed. The total incident radiation in each cell can be described as the sum of the incident radiation across all control angles and gray gases:

$$G_j = \sum_{l=1}^L I_{lj} \cdot \Delta\Omega_l, \quad (4)$$

where L is the total number of control angles. The radiative source for each gray gas is solved independently, and the total radiative source term is the sum of each gray gas contribution in the participating medium, which is calculated by²⁷:

$$S_{rad} = \sum_{j=1}^J \kappa_j (G_j - 4\sigma T^4), \quad (5)$$

where J is the total number of gray gases. The radiative source term in Equation (5) is implemented as a source term in the enthalpy transport equation. The boundary condition for an opaque nonreflecting wall may be written as follows²⁷:

$$I_{bnd}^l = \epsilon \frac{\sigma T^4}{\pi} + (1 - \epsilon) \frac{\sum_{(s_l \cdot n_w) > 0} I_{lj} |n_i D_{ci}|}{\sum_{(s_l \cdot n_w) < 0} n_i D_{ci}}, \quad (6)$$

where ϵ denotes the wall emissivity, which is assumed to be 1, n_w is the outer wall unit vector, D_{ci} denotes auxiliary terms that depend on the orientation of the face wall and the control angle. Additionally, cyclic boundary conditions are applied to two IC engine boundaries, such that the outgoing radiation intensity values that exit the calculation domain through a cyclic boundary are set equal to the incoming radiation intensities entering the

domain at the other cyclic boundary. The convergence of RTE is reached when the difference between the new and the last iteration is less than 0.01%.

For the calculations with the SLW model, several gray gases are utilized as the replacement for non-gray gas, where each contribution is symbolized with the supplemental absorption cross-section $\bar{C}_{abs,j}$ and correlate the weight of gray gas a_j . The absorption cross-section ranges between 3×10^{-5} and $60 \text{ m}^2 \text{ mol}^{-1}$ for water vapor, while for CO_2 , the range is between 3×10^{-5} and $120 \text{ m}^2 \text{ mol}^{-1}$.³⁹ These limits of the absorption cross-sections, C_{\min} and C_{\max} are used for the calculation of a supplemental absorption cross-section $\bar{C}_{abs,j}$ of each gray gas:

$$\bar{C}_{abs,j} = C_{\min} \left(\frac{C_{\max}}{C_{\min}} \right)^{\frac{j}{J}}. \quad (7)$$

The absorption cross-section domain is divided into intervals equally spaced on a logarithmic scale, and the range between two consecutive supplemental absorption cross-sections, $\bar{C}_{abs,j}$ and $\bar{C}_{abs,j+1}$, treated as an independent gray gas, whose absorption cross-section $C_{abs,j}$, is defined as follows:

$$C_{abs,j} = \sqrt{\bar{C}_{abs,j} \bar{C}_{abs,j+1}}. \quad (8)$$

The gray gas weights, a_j can be obtained from the absorption-line blackbody distribution functions F , which is determined by the high-resolution HITRAN database that accounts for the radiative participation of CO_2 and H_2O .³⁹ The distribution function F is defined as:

$$F(C_{abs,j}) = \frac{\pi}{\sigma T^4} \int_{\{\eta: C_{\eta,j} < C_{abs,j}\}} I_{b\eta}(T) d\eta, \quad (9)$$

where the integral is calculated over the spectral wavenumber η . The weight of the j^{th} gray gas can be calculated as the difference distribution function F at the supplemental cross-section interval limits:

$$a_j = F(\bar{C}_{abs,j+1}) - F(\bar{C}_{abs,j}). \quad (10)$$

The combined absorption coefficient of CO_2 and H_2O , $\kappa_{\text{CO}_2+\text{H}_2\text{O}}$ is defined as the sum of the contributions of the two species²⁷:

$$\kappa_{\text{CO}_2+\text{H}_2\text{O}} = N_{\text{H}_2\text{O}} C_{abs,k,\text{CO}_2} + N_{\text{H}_2\text{O}} C_{abs,k,\text{CO}_2}, \quad (11)$$

where N is the molar density of the gas, which is determined from the local cell temperature and the species mass fraction.

In this work, 10 gray gases were used to compute non-gray radiative properties used in the SLW model. For the calculation of soot participation in radiative transport, the gray gas absorption model is assumed, due to its smoothly varying radiative properties, with the following equation⁴⁰:

$$\kappa_s = 0.672 Tc. \quad (12)$$

In Equation (12), the term c denotes the mass fraction of soot. For calculating the total absorption coefficient, the absorption coefficient of the soot is added to the combined absorption coefficient of CO₂ and H₂O, as shown in Equation (13).

$$\kappa_j = \kappa_{CO_2+H_2O} + \kappa_s. \quad (13)$$

2.2 | Combustion and pollutants emission modeling

A coherent flame model, ECFM-3Z combustion model, was employed for the modeling of the combustion process. The ECFM-3Z combustion model governing equations can be found in Jurić et al.,⁴¹ where the ECFM-3Z was also used for the modeling of combustion inside a combustion chamber of an industrial diesel engine. The constant autoignition and mixing parameters were assumed to have the default value of 1.

For the calculation of turbulence chemistry interaction (TCI), Probability Density Function (PDF) approach was considered in this work, which equations and details can be found in Ozen et al.²⁰ PDF is based on the presumed standard Gaussian PDF, where the temperature T is assumed to be the sum of mean temperature and temperature variance.

$$T = \bar{T} + x \sqrt{\overline{T'T'}}. \quad (14)$$

The mean value of the temperature function was calculated as approximate quadrature formula,

$$\overline{f(T)} \approx \sum_{k=1}^n \left(\bar{T} + x_k \sqrt{\overline{T'T'}} \right) c_k. \quad (15)$$

The temperature variance was calculated by solving its transport equation with its correction factors in each node

$$\begin{aligned} & \frac{\partial}{\partial t} (\rho \overline{T'T'}) + \frac{\partial}{\partial x_i} (\rho \tilde{u}_i \overline{T'T'}) \\ & = \frac{\partial}{\partial x_i} \left(\frac{20}{17} \mu_t \frac{\partial \overline{T'T'}}{\partial x_i} \right) + 2.86 \mu_t \left(\frac{\partial \bar{T}}{\partial x_i} \right)^2 - 2 \rho \frac{\varepsilon}{k} \overline{T'T'}. \end{aligned} \quad (16)$$

Furthermore, the spray process was modeled by the Euler Lagrangian approach. The liquid phase of an injected droplet is modeled as parcels, and the gas phase is modeled as a continuum. For each parcel, trajectories are calculated from the deceleration of injected droplets due to the drag force, where drag coefficient C_D is calculated by Schiller Naumann drag law:

$$m_p \frac{du_{pi}}{dt} = 0.5 \pi r^2 \rho C_D u_i^2. \quad (17)$$

The Euler Lagrangian model assumes spherical symmetry, uniformity, and liquid-vapor thermal equilibrium of all droplets. Additionally, the quasi-steady and uniform surrounding around the droplets is assumed. The breakup model of the droplet parcel is modeled with the Wave breakup model, where the droplet disintegration is calculated by:

$$\frac{dr}{dt} = - \frac{\lambda_w \Omega (r - 0.61 \lambda_w)}{3.726 r C_2}. \quad (18)$$

Further description of Wave breakup model is described in the literature.⁴² The constant C_2 of Wave model that dictates the breakup time of parcels specific for each injector system is set to 18. The half of nozzle diameter is assumed for the initial radius of droplet parcels. The Abramzon model was employed to model fuel evaporation, which governing equation can be found in Abramzon and Sirignano.⁴³ In recent publications, such a model has also been applied to calculate the multi-component evaporation process.⁴⁴

Special attention has been given to the NO_x and soot formation process. The Extended Zeldovich Model was employed for thermal NO emissions,⁴⁵ while a kinetic soot model was employed for the soot formation process. The prompt NO formation process in this work was calculated by employing the de Soete model, as in Cao et al.⁴⁶ The method described in Vujanović et al.⁴⁷ was used to determine the temperature fluctuations. The kinetic soot model is based on the detailed soot oxidation and agglomeration model. The source term calculation is determined from the PDF of the mixture fraction,^{48,49} which is a function of the scalar dissipation rate, pressure, and temperature on the oxidizer side. The surface growth, oxidation, particle inception, and fragmentation are considered to calculate of soot volume fraction.

3 | EXPERIMENTAL DATA AND NUMERICAL SETUP

The experimental validation data of the compression ignition engine was acquired from AVL GmbH.⁵¹ In

Table 1, the engine and injector properties are presented. For the generating computational mesh domain, the automatic mesher AVL ESE Diesel tool is employed. The observed engine features a ω -shape piston bowl, which denotes the shape of the combustion chamber, and by its shape, promotes combustion. Figure 1 shows a 1/8th segment of a cylinder with generated boundary selections at the top dead center (TDC), respectively 720°CA is demonstrated. In this work, simulations only for one eight engine cylinder were calculated since the fuel injector possesses eight nozzle orifices. A piston rim compensation volume is generated to satisfy the compression ratio for all discrepancies and leakage present in the actual experimental engine, as shown in Figure 1.

The simulation cycle was modeled from 610 to 860°CA , where the segment cyclic inlet boundary conditions were used for segment selections. Mesh movement is described with mesh rezoning procedure, compression, and expansion stroke, generated by the automatic mesher. The liquid fuel properties greatly influence spray integration and evaporation.⁵¹ Therefore, the injected liquid fuel used in the experiment Diesel EN590 B7 was defined with polynomial terms in FIRE. The B7 in the name of fuel indicates around 7% biodiesel content, which indicates the utilization of biofuels in conventional diesel engines.⁵² The injection rate timing has a direct

influence on engine performance,⁵³ for that reason, the inlet fuel velocity is calculated from the measured injection rate, which is shown in Figure 2. Figure 2 shows the injection curve rate is shown as a nondimensional parameter, where the area under the curve presents the total injected fuel mass in one operating cycle. The first introduced parcels that enter the domain are assumed to have the diameter same as the orifice diameter, 0.1 mm.

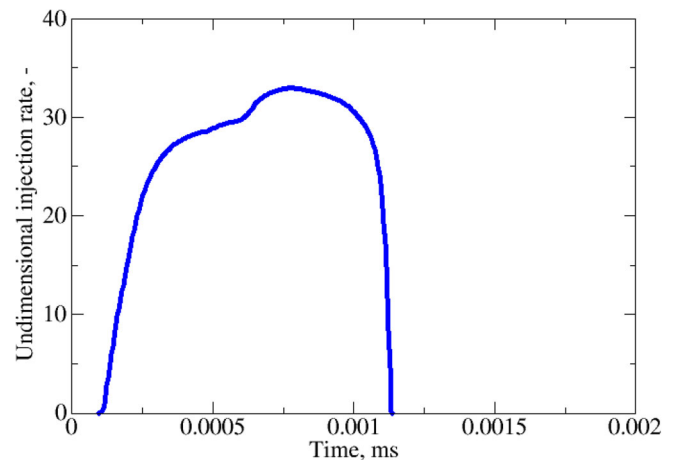


FIGURE 2 Injection rate profile of both observed operating points

TABLE 1 Experimental engine and injection system properties

Bore	85 mm	Injector position	(0, 0, -3.8) mm
Stroke	94 mm	Injector direction	(0, 0, 1)
Compression ratio	16	Spray angle	158°
Injected pressure	1200-1600 bar	Spray cone angle	15°
Fuel	Diesel EN590 B7	Number of nozzle holes	8
Fuel temperature	47°C	Nozzle hole diameter	100 μm
		Nozzle diameter at hole center position	4 mm

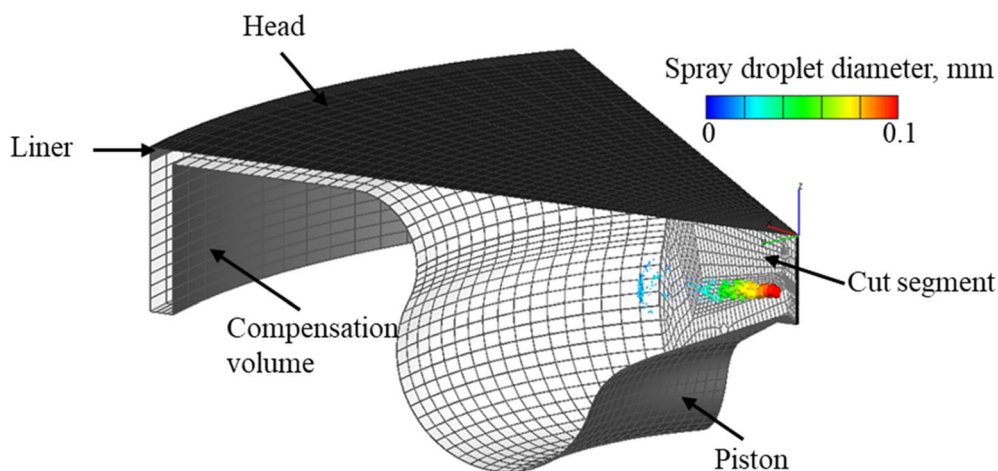


FIGURE 1 Computational engine mesh at the top dead center with the position of spray injector

In Table 2, boundary conditions for engine selections in Figure 1 are shown. Piston, liner, and headwall selections were modeled by an isothermal boundary condition, in which temperatures are obtained from the experimental analysis. For the compensation volume, an isolated boundary condition was assumed.

A mesh dependency study was performed to prove the validity of the generated mesh for simulations. Therefore, three hexahedral meshes with identical block cell structures were generated by varying the cell size. The total number of cells at the TDC position for the hexahedral generated meshes is shown in Table 3. All computational meshes are generated with a two-cell boundary layer to secure a correct calculation of the wall intensities. The simulations with the identical numerical

setup were performed for the three meshes, and the mean pressure results were compared. Figure 3 shows the computed and measured mean in-cylinder pressure from 700°CA, slightly before fuel injection, up to 750°CA. The coarse mesh is selected for all the simulations presented in this paper based on the mesh dependency analysis. The three generated moving meshes consist of 20 deformable meshes alternately mapped with the crank angle rotation. The rezoning procedure was implemented to be called when the physical quantities are mapped to the next mesh. After the multiprocessing finish with a calculation for crank angle time where the rezoning procedure is needed, the new mesh division on each processor is performed. The transfer of radiation quantities at the nodes of the next mesh is inherited from the precedent mesh.

TABLE 2 Boundary conditions

Boundary condition	Type	Description
Head	Wall	Isothermal, 500 K
Liner	Mesh movement/wall	Isothermal, 410 K
Compensation volume	Mesh movement/wall	Adiabatic
Cut segment	Inlet/outlet	Periodic
Piston	Wall	Isothermal, 500 K

TABLE 3 Number of cells at top dead center for the three generated meshes

Mesh	Cell number at the top dead center
Coarse	~24 000
Medium	~45 000
Fine	~63 000

In this work, two operating points are observed, Case *a* and Case *b*. The initial conditions and gas-phase composition of fresh air and exhaust gas residuals (EGR) differ for these two cases and are given in Table 4. Case *a* and Case *b* differ slightly in initial temperature, pressure and gas composition, and swirl motion inside the combustion chamber, while the injected mass in a single injection was approximately the same. Additionally, the main difference between the two cases is that Case *a* features an earlier injection than Case *b*.

For the combustion process modeling, the combustion parameters for autoignition and mixing of ECFM-3Z were used with default values, while for the Abramzon evaporation model, Lewis number was one.

In determining the radiative source term, each contribution of each control angle to radiative heat transfer needs to be accounted.⁵⁴ For the FVM model, the initial number of control angles is required, which affects the accuracy and computational demand of the calculations.⁵⁵ In this work, a selected number of control angles

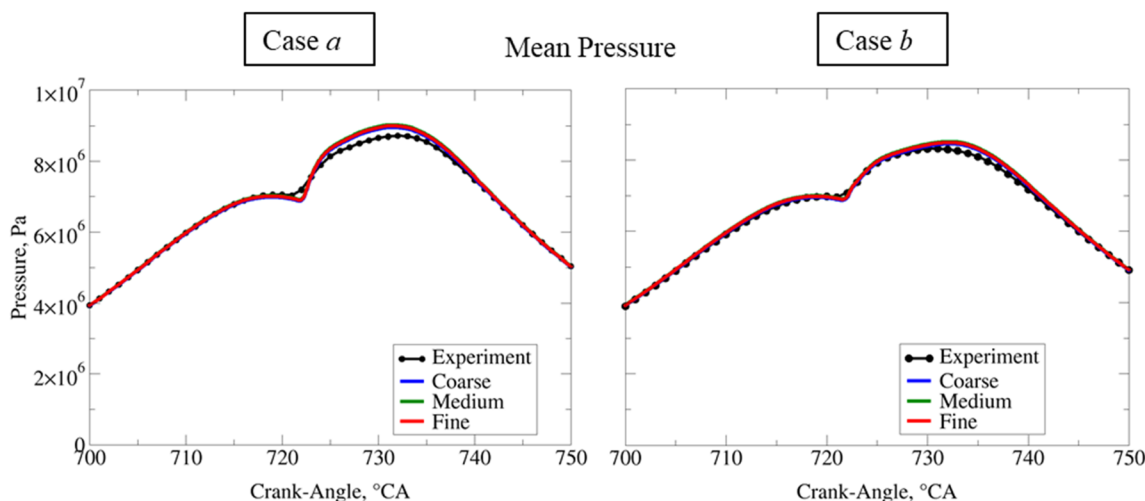


FIGURE 3 Mesh dependency results for three different meshes of the same block geometry

TABLE 4 Initial conditions and gas-phase composition

	Case a	Case b
Engine speed (rpm)	3000	3000
Number of injections	1	1
Injected mass (mg)	3.38	3.37
Pressure (Pa)	250 000	235 000
Temperature (K)	423	415
Swirl (1/min)	5403	5832
Start of injection (°CA)	712.5	713.5
End of injection (°CA)	735.4	734.8
Gas composition (kg/kg)		
O ₂	0.2085	0.2030
N ₂	0.7632	0.7620
CO ₂	0.0196	0.0243
H ₂ O	0.0087	0.0117

was eight after the control angle sensitivity analysis on temperature traces was performed. For the number of gray gases in the SLW model, calculations with 10 gray gases were observed, while the model assumes the spectral dependent absorption coefficient of the participating species. In Chai et al.,⁵⁶ the algorithm that calculates spatial discretization and control angles in this work is demonstrated. An emissivity value of unity was assumed for all wall boundaries. To save computational time, the radiative heat transfer solver was calculated for each 10th fluid flow iteration. This paper neglected the scattering due to the relatively small reflectivity of soot particles inside a chamber of IC engines, as was the case in Fernandez et al.⁵⁷

For calculating the momentum differencing scheme, the central differencing scheme was used for the momentum equation and continuity equation, while the upwind scheme was used for radiative heat transfer, turbulence parameters, total energy, and scalar conservation equations. The convergence criteria were set to residual values below 10^{-4} . For the time discretization, a dynamic time step was employed, where each new time step was calculated from Courant-Friedrichs-Lewy (CFL) condition. The maximum CFL number was set to 1. The SIMPLE algorithm calculated the coupling between pressure and velocity for solving the pressure correction equation.

3.1 | Validation of SLW model

The implemented absorption coefficient SLW model is validated on one-dimensional cases with an analytical solution. Two one-dimensional cases were selected for

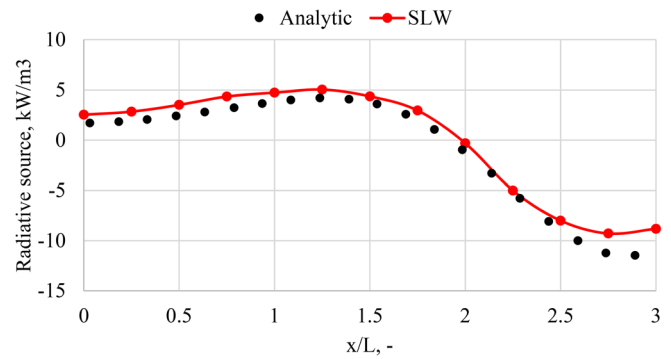


FIGURE 4 Radiative source profile results for the first validation case

which the predefined temperature and mole fraction of CO₂ and H₂O are shown in.²⁷ A hexahedral mesh of cubic cells $3 \times 3 \times 300$ was generated, where the profile is observed for the enclosed cell layer along the mesh axis.

In the nondimensional coordinate \tilde{x} is defined as:

$$\tilde{x} = \frac{\pi x}{L}, \quad (19)$$

where x is the position in the coordinate system, and L is the total length. Figure 4 shows the comparison of SLW against the analytical radiative source term for the first validation case in Table 5, where a good agreement is achieved for the trigonometric temperature profile with the SLW model. In Figure 5, the validation is shown for the second validation case in Table 5. Compared to the first validation case, the molar ratio of CO₂ and H₂O is also described with the trigonometric profile. The presented results in Figure 6 show that the simulation results insignificantly change when more control angles were applied to the numerical simulations. Based on the performed validation, it can be stated that the implemented SLW model is valid for describing the CO₂ and H₂O gas radiative properties.

4 | RESULTS AND DISCUSSION

This section discusses model validation, analysis of control angles, IC engine results, computational time, and specific conclusions and objectives of the paper.

4.1 | Results on compression ignition engine

Figure 6 compares temperature profiles for Case a and Case b. The orange curves show the numerical results

calculated with eight control angles, the green curve shows 16 control angles, and the violet curve for 32 control angles in the FVM radiation model. Experimental data are also presented as a reference, which indicates a better agreement of 32 control angles at the ignition phase of the combustion process. In comparison, the lower temperatures at eight control angles show a better matching in the developed combustion process. From the presented results in Figure 6, the simulation results insignificantly change when more control angles were applied

TABLE 5 Specifications of the two validation cases²⁷

	T, K	Y _{H2O}	Y _{CO2}	ϵ, —
1.	1000 + 250 cos(x̄)	0.1	0	1
2.	1000 - 300 cos(2x̄)	0.5 - 0.5 cos(x̄)	0.5 + 0.5 cos(x̄)	1

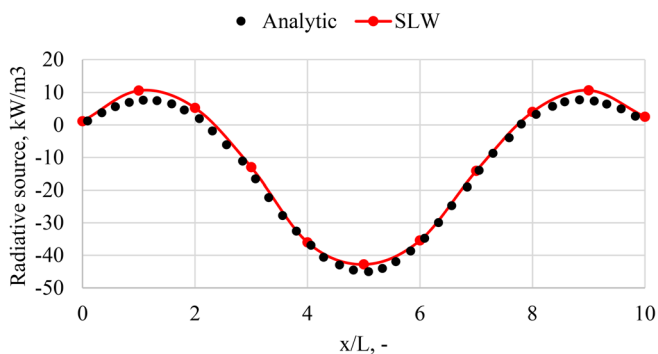


FIGURE 5 Radiative source profile results for the second validation case

to the numerical simulations. For that reason, all simulations in this work are computed with eight FVM control angles. A similar influence of control angle number on the simulation results is noticeable in both cases.

Figure 7 shows the mean pressure in the cylinder, mean temperature, and rate of heat release (RoHR) results for Case *a* and Case *b*. The RoHR results are shown for computational mesh, an eighth of an engine combustion chamber. The black lines with dots are experimental data, blue curves are results without considering radiation heat transport, and orange curves result from the implemented SLW model. For all results, a more significant discrepancy between SLW results and results without radiation is achieved for Case *a*, while for Case *b*, the later ignition time results in lower mean pressure, mean temperature, and RoHR results. The difference in the ignition delay between results with and without radiation is visible in Figure 7, associated with the different radiative absorption coefficient values. The radiative absorption energy of CO₂ and H₂O is approximately similar in Case *a* and Case *b*, which can be prescribed to their similar gas composition and thermodynamic conditions. Although the difference between the calculated impact of the radiation between Case *a* and Case *b* is visible in Figure 7. That is why the difference between results with SLW and without radiative heat transfer can be prescribed primarily to the absorption of soot particles, which have gray gas behavior. As expected, the radiative absorption of a large share of incident radiative flux is the largest in the regions of high temperatures. Overall, more accurate results and better agreement with experimental data were achieved with the SLW model, which considers the additional spectral phenomenon of radiative heat transport.

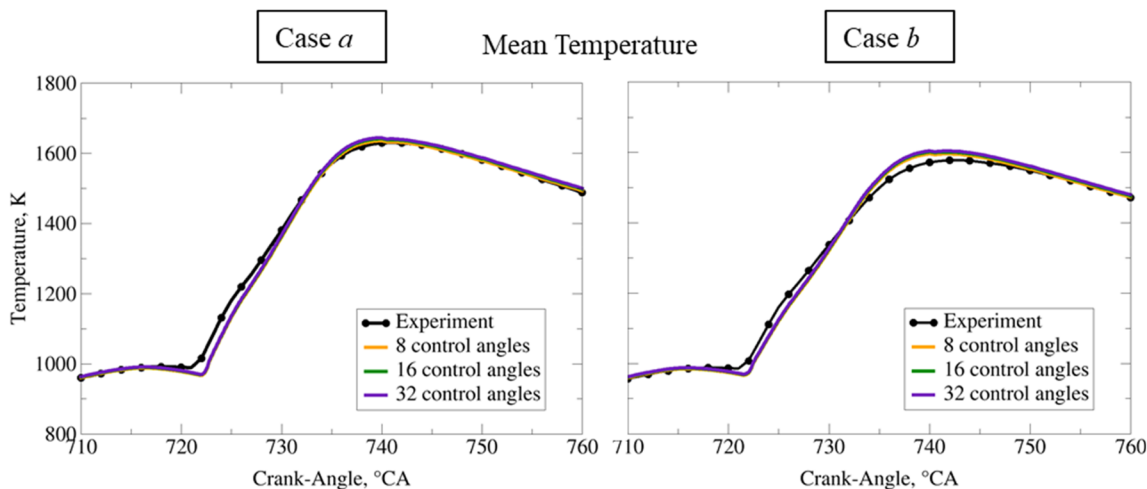


FIGURE 6 Mean temperature results for Case *a* and Case *b* with SLW model and different number of control angles in FVM radiation model

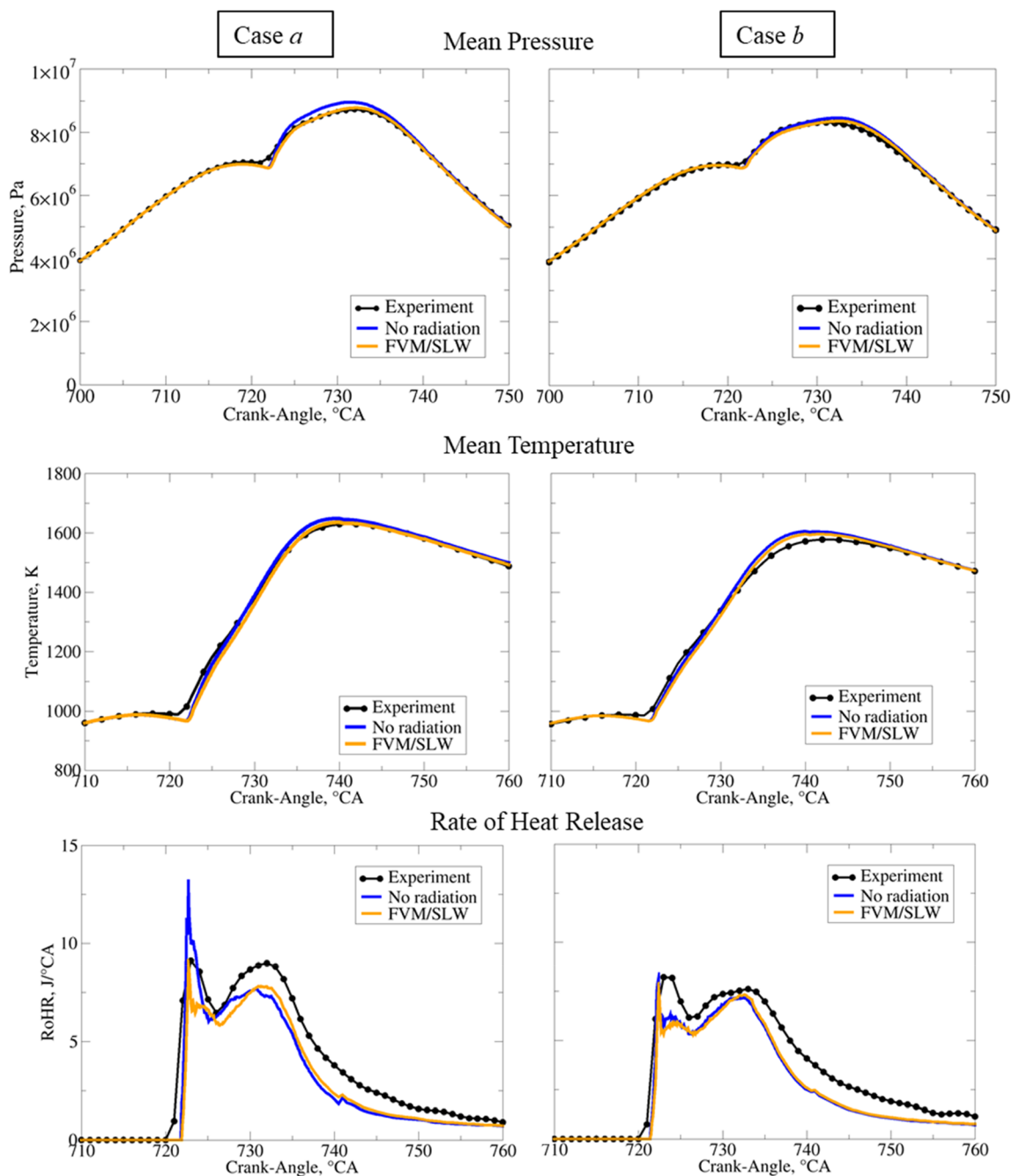


FIGURE 7 Mean in-cylinder pressure results, mean temperature, and RoHR results for Case *a* (left) and Case *b* (right) with SLW model and without radiation against experimental results

4.2 | Emission results

Comparing experimental results and simulations with and without radiation is given in Table 6 for pollutant emissions at the crank angle position when the exhaust valve opens. The results show that the radiative heat transport improves the predictions, leading to a better agreement with the experimental data. Table 6 shows that the soot mass fraction increases when the radiative heat transport is included. This indicates that the lower

temperatures in simulations with included radiative heat transfer result in a pronounced decrease in oxidation temperature vs the reduction in soot production. In contrast, the NO concentrations decrease, which are significantly generated by high-temperature regions. All predictions with the SLW accounting for radiation improve the prediction of NO emissions, which are of the same order of magnitude as the experimental data. It can be seen from Figure 7 that the tremendous difference between SLW and results without radiation is present in

TABLE 6 Pollutant mass ratio in the exhaust system

	Experiment	No radiation	SLW
Case a			
Soot (ppm)	899	273	356
NO (ppm)	309	512	417
Case b			
Soot (ppm)	2462	512	985
NO (ppm)	196	217	205

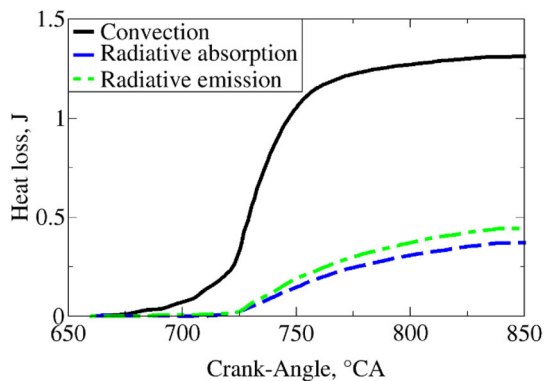


FIGURE 8 Convective, radiative absorption, and radiative emission heat losses for Case b

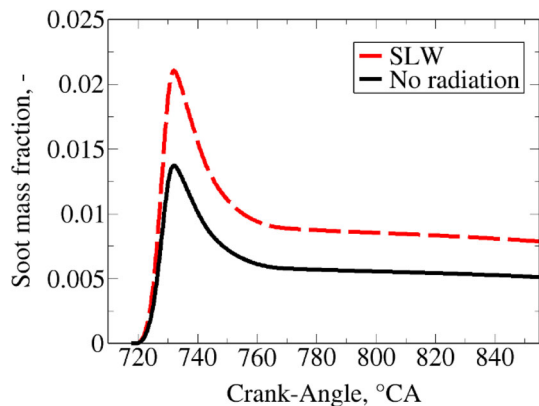


FIGURE 9 Soot mass fraction profile for Case b

Case a, which can be mainly attributed to the gray gas soot assumption. The lower soot absorption indicates that the soot oxidation is pronounced in Case a since both cases have similar initial composition and the approximately same amount of injected fuel. The pronounced soot oxidation processes also correspond to higher calculated temperatures in Case a. For the last two columns in Table 6, the results with and without including TCI are compared. The exhaust pollutant molar mass.

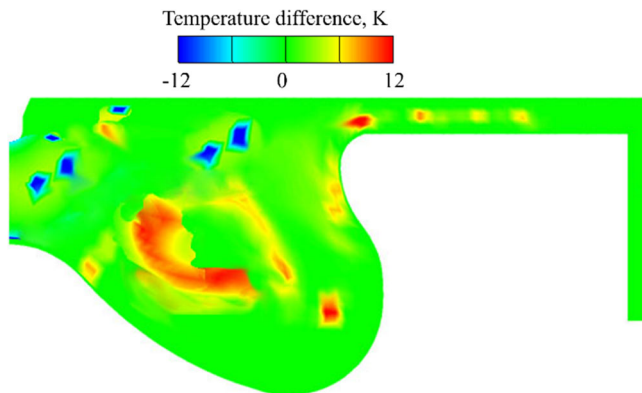


FIGURE 10 Temperature difference between results with SLW and without radiation at the crank-angle position with peak soot values (732°CA) for Case b

TABLE 7 Computational time for Case a on 10 control processing units of Intel Xeon E5-2650 v4 at 2.20 GHz

Calculation time, min	No radiation	SLW
Case a	34	70
Case b	31	68

Figure 8 shows calculated heat loss profiles for different crank angle positions for Case b. The heat losses are calculated through the wall boundary layer, where 9.5% of the total fuel energy is lost due to the convective losses. In comparison, the net radiative loss due to the higher emission than absorption of participating CO₂ and H₂O gasses is approximately 7% to 8% of convection heat loss. In Figure 9, the profiles of soot mass fraction for the simulation with and without including radiative heat transfer are shown, with the following Figure 10 shows temperature difference contour at the crank angle position with peak soot concentration, 732°CA. The interaction between soot concentrations and radiative heat transfer does not have a simple influence as with NO formation. The soot for the obtained results is mainly influenced by the regions of lower temperatures computed by SLW simulations, which were dominant compared to the regions with lower temperatures, as shown in Figure 7. The higher temperature differences correlate to the fuel-rich regions along high-temperature regions. The area of highest difference is around the equivalence ratio values of 2 to 3, where the neighbor cells are already ignited and consumed their oxygen.

In Table 7, the difference in the computational requirements of the simulations is shown. The computational time increases around two times when thermal radiation is considered, which is related to the additional

10 transport equations per control angle for each gray gas that needs to be solved in FVM/SLW.

5 | CONCLUSION

The SLW model was coupled with FVM radiation solver and implemented by programable user routines in the CFD software AVL FIRE. The implemented SLW model is based on correlations for unequal temperatures and mixtures of H₂O, CO₂, and soot, and the solver to RTE was modified to account for the spectral gas properties with absorption cross-sections and associated weight of gray gases. The soot absorption was assumed as gray gas absorption, while the implementation of boundary conditions is performed for diffusely reflective walls, periodic inflow/outflow, and symmetry. The model was implemented for application to parallel computing, moving meshes, and rezoning processes to be suitable for calculating radiative heat transfer in IC engines. The implemented SLW model achieved a good matching with one-dimensional validation cases with the analytical radiative heat transfer solution. Additionally, this investigation in this work emphasizes the combined radiation heat transport and combustion characteristics in a compression ignition. The predicted results of the in-cylinder pressure, temperature, and RoHR are significantly corresponding with the experiment data. As expected, the most decisive influence of the radiation transport in participating media is visible at crank positions with the highest pressures and temperatures, where the highest difference between simulations with SLW and with no radiation is obtained. The main difference between SLW and results without radiation arises at peak temperatures, where the gray gas soot assumption is its primary cause. The soot concentrations at the exhaust exit are increased with the SLW model, which could be prescribed to the lower temperatures that indicate a predominant decrease of soot oxidation vs the decrease in soot production. The higher temperature differences indicate that the soot regions are located in the fuel-rich regions along high-temperature regions. In contrast, the NO concentration emissions decrease with the inclusion of radiation in simulations, where the decrease is more pronounced with the more significant difference between the experiment and the simulation without radiation. The calculated heat convective losses through the wall boundary layer were 9.5% of the total fuel energy, while the net radiative loss due to the higher emission than absorption of participating CO₂ and H₂O gasses is 7% to 8% of convection heat loss. The soot production in both operating cases is approximately doubled, while the trend of soot production is achieved for simulations with included radiation and without radiation.

The computational time is around two times more demanding with the SLW model than in simulation without radiation, which is correlated to additional 10 transport equations for each gray gas in the SLW model. Finally, it can be concluded that the presented method can serve as a solution for more physically correct predictions of the radiation heat transport in compression ignition engines. Although in the case of large IC engines, such as big trucks or large ships, the role of thermal radiation is expected to become relevant due to the larger cylinder volume. Future work is to investigate results in the operating cases with higher EGR values accounting for the turbulence radiation interaction.

ACKNOWLEDGEMENTS

This work was funded under the auspice of the European Regional Development Fund, Operational Programme Competitiveness and Cohesion 2014–2020, KK.01.1.1.04.0070.

DATA AVAILABILITY STATEMENT

Data openly available in a public repository that issues datasets with DOIs.

ORCID

Filip Jurić  <https://orcid.org/0000-0002-9579-2949>

REFERENCES

1. Krishnamoorthy G, Jimenez M. Non-gray modeling of radiative heat transfer in hydrogen combustion scenarios. *Int J Energy Res.* 2012;36:789-797. doi:10.1002/er.1836
2. López Pérez S, Herrero López S, Ubieta Astigarraga E, et al. Design of a radiant heat capturing device for Steel Mills. *J Sustain Dev Energy Water Environ Syst.* 2021;9:1-15. doi:10.13044/j.sdewes.d8.0365
3. Paul C, Ferreyro Fernandez S, Haworth DC, Roy S, Modest MF. A detailed modeling study of radiative heat transfer in a heavy-duty diesel engine. *Combust Flame.* 2019;200:325-341. doi:10.1016/j.combustflame.2018.11.032
4. Dimitriadis A, Seljak T, Vihar R, et al. Improving PM-NO_x trade-off with paraffinic fuels: a study towards diesel engine optimization with HVO. *Fuel.* 2020;265:116921. doi:10.1016/j.fuel.2019.116921
5. Fujimori T, Hamano Y, Sato J. Radiative heat loss and NO_x emission of turbulent jet flames in preheated air up to 1230 K. *Proc Combust Inst.* 2000;28:455-461. doi:10.1016/S0082-0784(00)80243-X
6. Lazaroiu G, Pană C, Mihaescu L, et al. Solutions for energy recovery of animal waste from leather industry. *Energ Conver Manage.* 2017;149:1085-1095. doi:10.1016/j.enconman.2017.06.042
7. Mikulčić H, Cerinski D, Baleta J, Wang X. Improving pulverized coal and biomass co-combustion in a cement rotary kiln by computational fluid dynamics. *Chem Eng Technol.* 2019;42:2539-2545. doi:10.1002/ceat.201900086
8. Józsa V, Hidegh G, Kun-Balog A, Ng J-H, Chong CT. Ultra-low emission combustion of diesel-coconut biodiesel fuels by a

- mixture temperature-controlled combustion mode. *Energy Convers Manage.* 2020;214:112908. doi:10.1016/j.enconman.2020.112908
9. Mikulčić H, Baleta J, Wang X, Wang J, Qi F, Wang F. Numerical simulation of ammonia/methane/air combustion using reduced chemical kinetics models. *Int J Hydrogen Energy.* 2021; 46:23548-23563. doi:10.1016/j.ijhydene.2021.01.109
 10. Paul C, Haworth DC, Modest MF. A simplified CFD model for spectral radiative heat transfer in high-pressure hydrocarbon-air combustion systems. *Proc Combust Inst.* 2019;37:4617-4624. doi:10.1016/j.proci.2018.08.024
 11. Modest MF. *Radiative Heat Transfer.* 4th ed. Oxford: Elsevier; 2021. doi:10.1016/B978-0-12-503163-9.X5000-0
 12. Coelho PJ. Radiative Transfer in Combustion Systems. *Handbook of Thermal Science and Engineering.* Cham: Springer International Publishing; 2018:1173-1199. doi:10.1007/978-3-319-26695-4_61
 13. Benajes J, Martin J, Garcia A, et al. An investigation of radiation heat transfer in a light-duty diesel engine. *SAE Int J Engines.* 2015;8:2199-2212. doi:10.4271/2015-24-2443
 14. Jurić F, Petranović Z, Vujanović M, Duić N. Numerical assessment of radiative heat transfer impact on pollutant formation processes in a compression ignition engine. *J Clean Prod.* 2020; 275:12308. doi:10.1016/j.jclepro.2020.123087
 15. Yue Z, Reitz RD. Numerical investigation of radiative heat transfer in internal combustion engines. *Appl Energy.* 2019;235: 147-163. doi:10.1016/j.apenergy.2018.10.098
 16. Juric F, Vujanovic M, Zivic M, Holik M, Wang X, Duić N. Assessment of radiative heat transfer impact on a temperature distribution inside a real industrial swirled furnace. *Therm Sci.* 2020;24:3672. doi:10.2298/TSCI200407285J
 17. Mazzei L, Puggelli S, Bertini D, Pampaloni D, Andreini A. Modelling soot production and thermal radiation for turbulent diffusion flames. *Energy Procedia.* 2017;126:826-833. doi:10.1016/j.egypro.2017.08.266
 18. Mishra SC, Chugh P, Kumar P, Mitra K. Development and comparison of the DTM, the DOM and the FVM formulations for the short-pulse laser transport through a participating medium. *Int J Heat Mass Transf.* 2006;49:1820-1832. doi:10.1016/j.ijheatmasstransfer.2005.10.043
 19. Coelho PJ. On the convergence of the discrete ordinates and finite volume methods for the solution of the radiative transfer equation. *ASME Verif Valid Symp.* 2013;145:121-146.
 20. Ozen G, Ates C, Selçuk N, Kulah G. Assessment of SLW-1 model in the presence of gray and non-gray particles. *Int J Therm Sci.* 2019;136:420-432. doi:10.1016/j.ijthermalsci.2018.10.038
 21. Modest MF, Haworth DC. Radiative heat transfer in high-pressure combustion systems. *SpringerBriefs in Applied Sciences and Technology.* Cham: Springer Verlag; 2016:137-148. doi:10.1007/978-3-319-27291-7_7
 22. Krishnamoorthy G. A new weighted-sum-of-gray-gases model for oxy-combustion scenarios. *Int J Energy Res.* 2013;37:1752-1763. doi:10.1002/er.2988
 23. Guo J, Shen L, Wan J, Li P, Liu Z. A full spectrum k-distribution-based weighted-sum-of-gray-gases model for pressurized oxy-fuel combustion. *Int J Energy Res.* 2021;45:3410-3420. doi:10.1002/er.6010
 24. Shan S, Zhou Z, Chen L, Wang Z, Cen K. New weighted-sum-of-gray-gases model for typical pressurized oxy-fuel conditions. *Int J Energy Res.* 2017;41:2576-2595. doi:10.1002/er.3838
 25. Denison MK, Webb BW. The spectral line-based weighted-sum-of-gray-gases model in nonisothermal nonhomogeneous media. *J Heat Transfer.* 1995;117:359-365. doi:10.1115/1.2822530
 26. Ozen G, Selçuk N. SLW model for computational fluid dynamics modeling of combustion systems: implementation and validation. *Numer Heat Transf Part B Fundam.* 2016;70:47-55. doi:10.1080/10407790.2016.1173499
 27. Garten B, Hunger F, Messig D, Stelzner B, Trimis D, Hasse C. Detailed radiation modeling of a partial-oxidation flame. *Int J Therm Sci.* 2015;87:68-84. doi:10.1016/j.ijthermalsci.2014.07.022
 28. Webb BW, Ma J, Pearson JT, Solovjov VP. SLW modeling of radiation transfer in comprehensive combustion predictions. *Combust Sci Technol.* 2018;190:1392-1408. doi:10.1080/00102202.2018.1452123
 29. Ali HB, Askri F, Ben NS. Comparative study of WSGG and SLW models coupled with control volume finite element method for non gray radiation prediction. *Int J Therm Sci.* 2017;113:73-82. doi:10.1016/j.ijthermalsci.2016.11.009
 30. Sun Y, Zhang X. Contributions of gray gases in SLW for non-gray radiation heat transfer and corresponding accuracies of FVM and P1 method. *Int J Heat Mass Transf.* 2018;121:819-831. doi:10.1016/j.ijheatmasstransfer.2018.01.045
 31. Yasar MS, Ozen G, Selçuk N, Kulah G. Assessment of improved banded model for spectral thermal radiation in presence of non-gray particles in fluidized bed combustors. *Appl Therm Eng.* 2020;176:115322. doi:10.1016/j.applthermaleng.2020.115322
 32. Payan S, Hosseini Sarvari SM, Behzadmehr A. Reconstruction of temperature distribution in the combustion region of a non-gray medium. *Numer Heat Transf Part A Appl.* 2015;68:908-924. doi:10.1080/10407782.2015.1023125
 33. Klason T, Bai XS, Bahador M, Nilsson TK, Sundén B. Investigation of radiative heat transfer in fixed bed biomass furnaces. *Fuel.* 2008;87:2141-2153. doi:10.1016/j.fuel.2007.11.016
 34. Ströhle J. Wide band correlated-k approaches for non-grey radiation modelling in oxy-fuel combustion with dry recycling. *Fuel.* 2011;90:3007-3013. doi:10.1016/j.fuel.2011.05.002
 35. Liu F, Consalvi JL, Coelho PJ, et al. The impact of radiative heat transfer in combustion processes and its modeling – with a focus on turbulent flames. *Fuel.* 2020;281:118555. doi:10.1016/j.fuel.2020.118555
 36. Webb BW, Solovjov VP, André F. The spectral line weighted-sum-of-gray-gases (SLW) model for prediction of radiative transfer in molecular gases. *Adv Heat Transf.* 2019;51:207-298. doi:10.1016/bs.aiht.2019.08.003
 37. Ozen G, Selçuk N. Sensitivity of radiation modeling to property estimation techniques in the freeboard of lignite-fired bubbling fluidized bed combustors (BFBCs). *Combust Sci Technol.* 2014; 186:684-697. doi:10.1080/00102202.2014.883848
 38. Hanjalić K, Popovac M, Hadžiabdić M. A robust near-wall elliptic-relaxation eddy-viscosity turbulence model for CFD. *Int J Heat Fluid Flow.* 2004;25:1047-1051. doi:10.1016/j.ijheatfluidflow.2004.07.005
 39. Pearson JT, Webb BW, Solovjov VP, Ma J. Efficient representation of the absorption line blackbody distribution function for H₂O, CO₂, and CO at variable temperature, mole fraction, and total pressure. *J Quant Spectrosc Radiat Transf.* 2014;138:82-96. doi:10.1016/j.jqsrt.2014.01.019
 40. Khalil EE, Truelove JS. Calculation of radiative heat transfer in a large gas fired furnace. *Lett Heat Mass Transf* 1977;4:353-65. doi:10.1016/0094-4548(77)90124-2

41. Jurić F, Stipić M, Samec N, Hriberšek M, Honus S, Vujanović M. Numerical investigation of multiphase reactive processes using flamelet generated manifold approach and extended coherent flame combustion model. *Energ Conver Manage*. 2021;240:114261. doi:10.1016/j.enconman.2021.114261
42. Dhuchakallaya I, Watkins AP. Application of spray combustion simulation in DI diesel engine. *Appl Energy*. 2010;87:1427-1432. doi:10.1016/j.apenergy.2009.08.029
43. Abramzon B, Sirignano WA. Droplet vaporization model for spray combustion calculations. *Int J Heat Mass Transf*. 1989;32:1605-1618. doi:10.1016/0017-9310(89)90043-4
44. Bešenić T, Baleta J, Pachler K, Vujanović M. Numerical modelling of sulfur dioxide absorption for spray scrubbing. *Energ Conver Manage*. 2020;217:112762. doi:10.1016/j.enconman.2020.112762
45. Bešenić T, Mikulčić H, Vujanović M, Duić N. Numerical modelling of emissions of nitrogen oxides in solid fuel combustion. *J Environ Manage*. 2018;215:177-184. doi:10.1016/J.JENVMAN.2018.03.014
46. Cao H, Sun S, Liu Y, Wall TF. Computational fluid dynamics modeling of NO_x reduction mechanism in oxy-fuel combustion†. *Energy Fuel*. 2010;24:131-135. doi:10.1021/ef900524b
47. Vujanović M, Duić N, Tatschl R. Validation of reduced mechanisms for nitrogen chemistry in numerical simulation of a turbulent non-premixed flame. *React Kinet Catal Lett*. 2009;96:125-138. doi:10.1007/s11144-009-5463-2
48. Karlsson A, Magnusson I, Balthasar M, Mauss F. Simulation of soot formation under diesel engine conditions using a detailed kinetic soot model. *J Engines*. 1998;107:1430. doi:10.4271/981022
49. Priesching P, Tatschl R, Mauss F, et al. Soot Particle Size Distribution~A Joint Work for Kinetic Modelling and Experimental Investigations. 2005. doi:10.4271/2005-24-053
50. Petranović Z, Bešenić T, Vujanović M, Duić N. Modelling pollutant emissions in diesel engines, influence of biofuel on pollutant formation. *J Environ Manage*. 2016;203:1-9. doi:10.1016/j.jenvman.2017.03.033
51. Csemány D, DarAli O, Rizvi SAH, Józsa V. Comparison of volatility characteristics and temperature-dependent density, surface tension, and kinematic viscosity of n-butanol-diesel and ABE-diesel fuel blends. *Fuel*. 2022;312:122909. doi:10.1016/j.fuel.2021.122909
52. Stančin H, Mikulčić H, Wang X, Duić N. A review on alternative fuels in future energy system. *Renew Sustain Energy Rev*. 2020;128:109927. doi:10.1016/j.rser.2020.109927
53. Sremec M, Taritaš I, Sjerić M, Kozarac D. Numerical investigation of injection timing influence on fuel slip and influence of compression ratio on Knock occurrence in conventional dual fuel engine. *J Sustain Dev Energy Water Environ Syst*. 2017;5:518-532. doi:10.13044/j.sdewes.d5.0163
54. Coelho PJ. Advances in the discrete ordinates and finite volume methods for the solution of radiative heat transfer problems in participating media. *J Quant Spectrosc Radiat Transf*. 2014;145:121-146. doi:10.1016/j.jqsrt.2014.04.021
55. Mishra SC, Roy HK. Solving transient conduction and radiation heat transfer problems using the Lattice Boltzmann method and the finite volume method. *J Comput Phys*. 2007;223:89-107. doi:10.1016/j.jcp.2006.08.021
56. Chai JC, Parthasarathy G, Lee HS, Patankar SV. Finite volume radiative heat transfer procedure for irregular geometries. *J Thermophys Heat Transf*. 1995;9:410-415. doi:10.2514/3.682
57. Fernandez SF, Paul C, Sircar A, et al. Soot and spectral radiation modeling for high-pressure turbulent spray flames. *Combust Flame*. 2018;190:402-415. doi:10.1016/j.combustflame.2017.12.016

How to cite this article: Jurić F, Coelho PJ, Priesching P, Duić N, Honus S, Vujanović M. Implementation of the spectral line-based weighted-sum-of-gray-gases model in the finite volume method for radiation modeling in internal combustion engines. *Int J Energy Res*. 2022;1-14. doi:10.1002/er.8177